Journal of Organometallic Chemistry 883 (2019) 52–64

Contents lists available at ScienceDirect

Journal of Organometallic Chemistry

journal homepage: www.elsevier.com/locate/jorganchem

A triple alkoxo bridged dinuclear cobalt(III) complex mimicking phosphatase and showing ability to degrade organic dye contaminants by photocatalysis

Kousik Ghosh [a], Klaus Harms [b], Antonio Franconetti [c], Antonio Frontera [c, **], Shouvik Chattopadhyay [a, *]

[a] *Department of Chemistry, Inorganic Section, Jadavpur University, Kolkata, 700032, India*
[b] *Fachbereich Chemie, Philipps-Universität Marburg, Hans-Meerwein-Strasse, D-35032, Marburg, Germany*
[c] *Departamento de Química, Universitat de les Illes Balears, Crta. de Valldemossa km 7.5, 07122, Palma (Baleares), Spain*

ARTICLE INFO

Article history:
Received 16 December 2018
Received in revised form
9 January 2019
Accepted 10 January 2019
Available online 11 January 2019

Keywords:
Cobalt(III)
Crystal structure
DFT calculation
Phosphatase mimicking activity
Photocatalytic degradation of methylene blue (MB)

ABSTRACT

A dinuclear cobalt(III) complex, $[(N_3)L^1Co^{III}L^2Co^{III}L^1]$ (**1**), has been synthesized and characterized {H_2L^1 = 2-((1-hydroxybutan-2-ylimino)methyl)-4-bromophenol and HL^2 = 2-amino-1-butanol}. Single crystal X-ray diffraction analysis confirmed its structure. Extended supra-molecular architectures were generated in the complex through weak noncovalent interactions. The energetic features of significant supramolecular interactions have been investigated using DFT calculation and further corroborated with NCI plot index computational tool. The complex has been found to mimic the role of phosphatase enzyme efficiently by transforming 4-nitrophenylphosphate to 4-nitrophenolate at room temperature. The reaction follows Michaelis–Menten enzymatic reaction kinetics with turnover numbers of ~1.4 s^{-1} in aqueous DMF (98% DMF, v/v) medium. The complex also acts as an efficient photocatalyst for degradation of organic pollutants. Methylene blue (MB), a widely used dye in various industries, was selected as a model pollutant in aqueous media to evaluate the photocatalytic effectiveness of the complex.

1. Introduction

Numerous dinuclear transition metal complexes have been found to have fascinating applications in molecular magnetism [1–3]. It is also interesting to explore whether the mode of bridging is influencing the physical properties of a dinuclear complex and, if yes, why [4–6]. Focusing to diamagnetic cobalt(III), magnetic characterization is only a routine work and is not at all interesting. However, dinuclear cobalt(III) complexes are attractive for their appealing applications in biological modeling [7,8] e.g. to mimic phosphatase. Phosphatase is a hydrolase enzyme that hydrolyses the P–O bond of a phosphoester substrate, thereby producing a phosphate ion and alcohol [9–11]. Cobalt(III) complexes may also be used as photocatalyst for the degradation of organic pollutants. The environmental pollution caused by organic pollutants (e.g. methylene blue, MB, a dye used in industry) is a huge problem in our time [12–14]. The majority of the coloured effluents identified in waste water are a consequence of organic dyes in textiles, dyestuffs, and dyeing industries [15,16]. It is not very easy to deal with them by the method of conventional waste water treatment because of their high solubilities in water. Therefore, photocatalysis are used for the green ecological elimination of these harmful pollutants [17–19].

Our laboratory has been actively engaged to design, synthesis and explore bio-relevant catalytic activities including phosphatase activity of several transition (e.g. iron, cobalt, copper, nickel etc) and non-transition metal (e.g. zinc) complexes for the last few years [19,20]. Recently, we have also worked on photocatalytic degradation of organic dye by zinc and cadmium complexes [29–32]. Many other groups are also working on these two topics [33–40]. However, to the best of our knowledge investigated complex is unique in the sense that it possess catalytic efficiency towards both hydrolysis of phosphoester linkage and photocatalytic degradation of methylene blue.

In this work, we have designed and synthesized a dinuclear alkoxo bridged cobalt(III) Schiff base complex, $[(N_3)L^1Co^{III}L^2Co^{III}L^1]$,

---

* Corresponding author.
** Corresponding author.
E-mail address: shouvik.chem@gmail.com (S. Chattopadhyay).

https://doi.org/10.1016/j.jorganchem.2019.01.006

which can efficiently mimic phosphatase enzyme and acts as a photocatalyst for degradation of MB in visible light irradiation. The complex has been characterized by elemental and spectral analysis and the structure of the complex has been confirmed by single crystal X-ray diffraction study. The energetic features of significant halogen and hydrogen bonding interactions in the solid state structure of the complex have been investigated using DFT calculation, and further corroborated with NCI plot index computational tool.

2. Material and methods

2.1. Starting materials and solvents

Starting materials and solvents used in this work were purchased from Sigma-Aldrich, India (now Merck, India) and were of reagent grade. They were used as received, without further purification. The entire syntheses and manipulations were carried out under aerobic conditions.

Caution!!! *Even though no troubles were experienced in this work, metal complexes containing azide salts* and organic ligands *are potentially explosive. Only a small amount of material should be prepared, and it should be handled with care.*

2.2. Preparation of $[(N_3)L^1Co^{III}L^2Co^{III}L^1]$

An acetonitrile solution (20 ml) of 2-amino-1-butanol (0.10 mL, ~1 mmol) and 5-bromosalicyldehyde (201 mg, ~1 mmol) was refluxed for ca. 1 h to prepare the precursor compound, H_2L^1. An acetonitrile-methanol (2:1) mixture (10 ml) of cobalt(II) acetate tetrahydrate (249 mg, ~1 mmol) was then directly added to it, followed by the addition of aqueous methanol solution (5 ml) of sodium azide (65 mg, ~1 mmol) with constant stirring. The stirring was continued for additional 4 h. After leaving the resulting solution in aerial condition to evaporate about half of the solvent, dark red prisms of the complex compound were formed. The crystals were isolated, washed with acetonitrile-methanol (2:1) mixture three times and dried in a vacuum desiccator using anhydrous $CaCl_2$.

Yield: 350 mg (~42%); based on cobalt(III). Anal. Calc. for $C_{26}H_{39}Co_2Br_2N_6O_{7.5}$ (FW = 833.31): C, 37.47; H, 4.72; N, 10.09%. Found: C, 37.5; H, 4.7; N, 10.1%. FT-IR (KBr, cm^{-1}): 1591, 1631, ($\upsilon_{C=N}$); 2021 (υ_{N3}); 2880-2962 ($\upsilon_{C\text{-}H}$); 3134 ($\upsilon_{N\text{-}H}$); 3402 ($\upsilon_{O\text{-}H}$). UV–Vis, λ_{max} (nm), [ε_{max} ($dm^3\ mol^{-1}\ cm^{-1}$)] (DMF), 264 (7.09×10^4), 315 (1.04×10^4), 410 (7.03×10^3), 540 (5.26×10^2).

2.3. Instrumentation details

Elemental analysis (carbon, hydrogen and nitrogen) was performed using a Perkin-Elmer 240C elemental analyzer. Infrared spectrum in KBr pellets (4500-500 cm^{-1}) was recorded using a PerkinElmer Spectrum Two FTIR spectrophotometer. Electronic absorption spectrum in acetonitrile medium was recorded on a JASCO V-630 UV–Vis spectrophotometer. Electrospray ionization mass spectra were recorded using Waters QTOF Micro YA263 mass analyzer.

2.4. Crystallographic data collection and refinement details

Data was collected with an STOE IPDS 2T diffractometer equipped with Mo-K_α radiation, a graphite monochromator (λ = 0.71073 Å) and an image plate detector using an oil-coated shock-cooled crystal at 100(2) K. Absorption effects were corrected semi-empirical using multiscanned reflexions (X-Area LANA) [41]. Cell constants were refined using 34957 of observed reflections of the data collection. The structure was solved by direct methods by using the program XT V2014/1 (Bruker AXS Inc., 2014) [42] and refined by full matrix least squares procedures on F^2 using SHELXL-2018/3 [43–45]. The non-hydrogen atoms have been refined anisotropically, carbon and nitrogen bonded hydrogen atoms were included at calculated positions and refined using the ‘riding model’ with isotropic temperature factors at 1.2 times (for CH_3 groups 1.5 times) that of the preceding atom. CH_3 groups were allowed to rotate about the bond to their next atom to fit the electron density. Solvent water was refined as rigid groups. Disorder was refined for carbon side chains of the ligands and solvent water. Absorption corrections were carried out using the SADABS program [46]. Crystallographic data collection and refinement parameters and data for the crystal are given in Table 1.

2.5. Theoretical methods

The geometries of the complex included in this study were computed at the M06-2X/def2-TZVP level of theory using the crystallographic coordinates apart from the positions of the hydrogen atoms, which have been optimized. For all calculations we have used the GAUSSIAN-09 program [47]. We have also used the Grimme's dispersion [48] correction as implemented in GAUSSIAN-09 program since it is adequate for the evaluation of noncovalent interactions where dispersion effects are relevant like σ-hole interactions. The basis set superposition error for the calculation of interaction energies has been corrected using the counterpoise method [49]. The NCI plot [50] isosurfaces have been used to characterize noncovalent interactions. They correspond to both favorable and unfavorable interactions, as differentiated by the sign of the second density Hessian Eigen value and defined by the isosurface color. The colour scheme is a red-yellow-green-blue scale with red for ρ^{+}_{cut} (repulsive) and blue for ρ^{-}_{cut} (attractive).

2.6. Hirshfeld surface analysis

Hirshfeld surface encircles that region of space adjoining a particular molecule in a crystal where the electron distribution of the promolecule exceeds that due to any other molecule [51–53]. Typically, Hirshfeld surface is represented by thousands of surface points obtained by triangulation, and two parameters d_i (distance from the surface to the nearest atom interior to the surface) and d_e

Table 1
Crystal data and refinement details of the titled complex.

Formula	$C_{26}H_{34}Br_2Co_2N_6O_5$,2.5($H_2$ O)
Formula Weight	833.31
Temperature (K)	100(2)
Crystal System	Triclinic
Space group	$P\bar{1}$
a(Å)	9.9077(3)
b(Å)	12.3035(5)
c(Å)	15.0006(5)
α(°)	67.692(3)
β(°)	75.076(3)
γ(°)	83.495(3)
d(calc) [g/cm^3]	1.693
μ [mm^{-1}]	3.513
F(000)	842
Total Reflections	21365
Unique Reflections	6926
Observed data[I > 2 σ(I)]	6121
No of parameters	483
R(int)	0.039
R1, wR2 (all data)	0.0491, 0.0958
R1, wR2 ([I > 2 σ(I)]	0.0424, 0.0926
Residual Electron Density (eÅ^{-3})	0.660, −0.882

(distance from the surface to the nearest atom exterior to the surface) convey information about relevant contact distances from each point. To construct a 2D fingerprint plot, the molecular Hirshfeld surface is first obtained using standard methods [54]. As described in several previous reports [55,56], the Hirshfeld surface of the complex and its associated 2D fingerprint plots [57–59] were calculated using Crystal Explorer software [60], with bond lengths to hydrogen atoms set to standard values [54].

2.7. Kinetic measurements for the hydrolysis of 4-NPP

In the kinetics studies, to evaluate phosphate ester bond cleavage, disodium 4-nitrophenylphosphate hexahydrate (4-NPP) has been used as substrate. The phosphate ester bond cleavage tendency of the complex has been detected spectrophotometrically at 25 °C by monitoring the time evolution of 4-nitrophenolate (λ_{max} ~ 425 nm) in aqueous DMF (98% DMF, v/v) medium where substrate (10^{-3} M) was at least in 100 equivalents of the catalyst (10^{-5} M). Additionally, to check the rate dependency on catalyst concentration, similar sets of experiments were performed at a fixed concentration of substrate with variable catalyst concentrations. Rate of the reaction was derived from the initial rate method, and the average initial rate over three independent measurements was recorded. Several kinetic parameters such as V_{max} (maximum reaction velocity), K_M (Michaelis constant), k_{cat} (turnover number) and k_{cat}/K_M (specificity constant) have been evaluated for hydrolysis of 4-NPP (phosphatase mimicking activity) of the complex. Kinetic parameters V_{max} and K_M evacuated directly from the various enzyme kinetic equations such as Michaelis-Menten kinetics equation, Lineweaver-Burk equation, Hanes equation and Eadie-Hofstee equation. The k_{cat} value is obtained by dividing V_{max} by the concentration of the complex used.

2.8. Photocatalytic measurement of organic dye degradation

The photocatalytic activity of the synthesized complex was evaluated using methylene blue (MB). Photocatalytic degradation of Methylene Blue (MB) in aqueous medium has been carried out in a typical method [30–32]. The photocatalytic degradation has been carried out separately with 100 mL of MB solution (15 mg l^{-1}) using the complex as catalyst. The mixture solution has been pretreated by magnetic stirring in the dark environment for 20 min to achieve adsorption–desorption equilibrium of MB on the catalyst surface. After attaining the equilibrium, 2 mL of sample was taken from the reaction mixture in an interval of 10 min and irradiated with UV–Vis light. The characteristic peak for MB (~600 nm) has been employed to monitor the photocatalytic degradation. After complete decolorization the catalyst was recollected through centrifugation and recycled it to check the stability and reusability of the catalyst.

3. Results and discussion

3.1. Synthesis of the complex

The precursor compound, H_2L^1, was synthesized by the condensation of 2-amino-1-butanol with 5-bromosalicyldehyde in acetonitrile medium following the literature method [20–29]. The precursor compound was not isolated and used directly for the synthesis of the cobalt(III) complex without any further purification. Addition of the methanolic solution of cobalt(II) acetate tetrahydrate in the acetonitrile solution of precursor compound (H_2L^1) followed by the addition of aqueous-methanol solution of sodium azide produced a dark brown coloured alkoxo-bridged dinuclear cobalt(III) complex, $[(N_3)L^1Co^{III}L^2Co^{III}L^1]$. The formation of the complex is shown in Scheme 1.

The amine ligand, HL^2, most probably originates *in situ* via hydrolysis of the precursor compound, H_2L^1. As sodium azide is sparingly soluble in methanol, we used a methanol-water mixture solution (4: 1) of it. This increased concentration of water might be responsible for the initiation of hydrolysis. A plausible mechanistic pathway of hydrolysis of precursor compound is shown in Scheme 2.

Single crystal X-ray class dark brown single crystals of the complex were obtained from the 1: 1 methanol–acetonitrile solution. Cobalt(II) is readily oxidised to cobalt(III) by aerial oxygen in presence of Schiff base like strong field ligand, as was also observed in several other cobalt-Schiff base complexes [20,22,24]. We have repeated the reaction under inert atmosphere, but no complex could be isolated.

3.2. Description of the solid-state structure

Single crystal X-ray crystallographic data analysis reveals that the complex crystallizes in the triclinic space group, $P\overline{1}$. A perspective view of the complex together with the selective atom numbering scheme is shown in Fig. 1. The structure determination reveals that the complex consists of a discrete dinuclear unit $[(N_3)L^1Co^{III}L^2Co^{III}L^1]$ along with two and half lattice water molecules. Selective bond lengths and angles are gathered in Tables 2 and 3, respectively.

The basal plane of cobalt centre, Co(1), consists of one imine nitrogen atom, N(1), one phenoxo oxygen atom, O(4) and one hydroxy oxygen atom, O(1) from a deprotonated Schiff base ligand, $(L^1)^{2-}$ and one bridging hydroxy oxygen atom, O(2) of another deprotonated Schiff base ligand, whereas the axial coordination sites are occupied by one terminal azide nitrogen atom, N(2) and one bridging hydroxy oxygen atom, O(3) which is a structural part of a deprotonated free amine moiety, $(L^2)^{-}$. The deviation of the coordinating atoms, N(1), O(4), O(2) and O(1), in the basal plane from the mean plane passing through them are 0.042(5), 0.001(3), 0.040(3) and −0.006(3) Å and that of Co(1) from the same plane is −0.0763(6) Å. On the other hand, the basal plane of other cobalt centre, Co(2), consists of one imine nitrogen atom, N(5), one phenoxo oxygen atom, O(5) and one hydroxy oxygen atom, O(2) from a deprotonated Schiff base ligand and one bridging hydroxy oxygen atom, O(3) of a deprotonated free amine moiety. The amine nitrogen atom, N(6), of the deprotonated free amine moiety and bridging hydroxy oxygen atom, O(1) of the deprotonated Schiff base constitute the axial plane of cobalt centre, Co(2). In this case, the deviation of the coordinating atoms, N(5), O(2), O(3) and O(5), in the basal plane from the mean plane passing through them are −0.010(4), 0.027(3), −0.012(3) and 0.025(3) Å and that of Co(2) from the same plane is −0.0296(5) Å.

A Co_2O_3 core is formed due to tri-μ-hydroxo bridging. Within the core bridging angles, Co(1)–O(1)–Co(2), Co(1)–O(2)–Co(2) and Co(1)–O(3)–Co(2), are 82.45(11)°, 83.82(10)° and 83.16(11)°, respectively. The distance between two cobalt centres, Co(1)···Co(2), is 2.5539(9) Å. It is important to note that each cobalt centre is showing distorted octahedral geometry. The distortion from ideal octahedral geometry for each cobalt centre is due to restrictions imposed by the ligand, as evidenced by the bite angles (Table 3). Saturated five-membered chelate rings, R(1) [Co(2)–O(2)–C(16)–C(17)–N(5)] and R(2) [Co(2)–O(3)–C(30)–C(31)–N(6)] are present in half chair conformation with puckering parameters [61,62] $Q = 0.514(5)$ Å, $\phi = 268.3(4)°$ for R(1) and $Q = 0.440(4)$ Å, $\phi = 273.9(4)°$ for R(2).

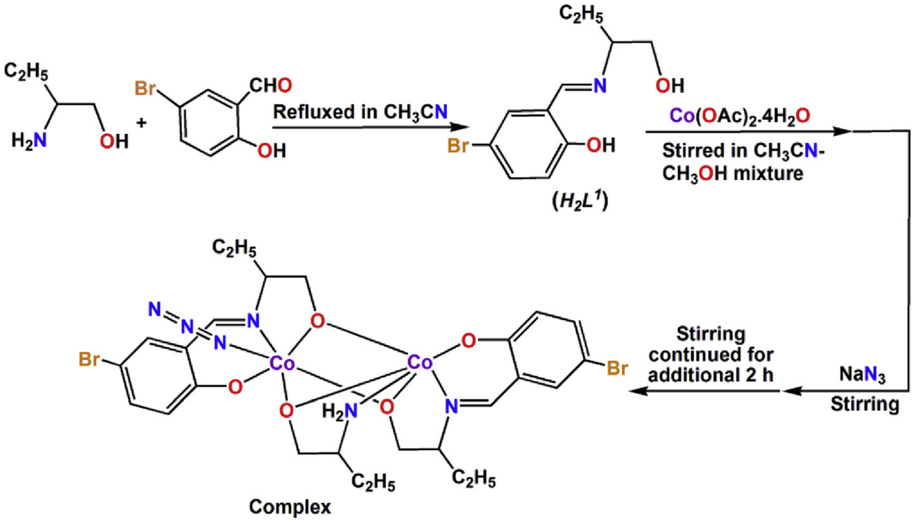

Scheme 1. Synthetic route to the complex.

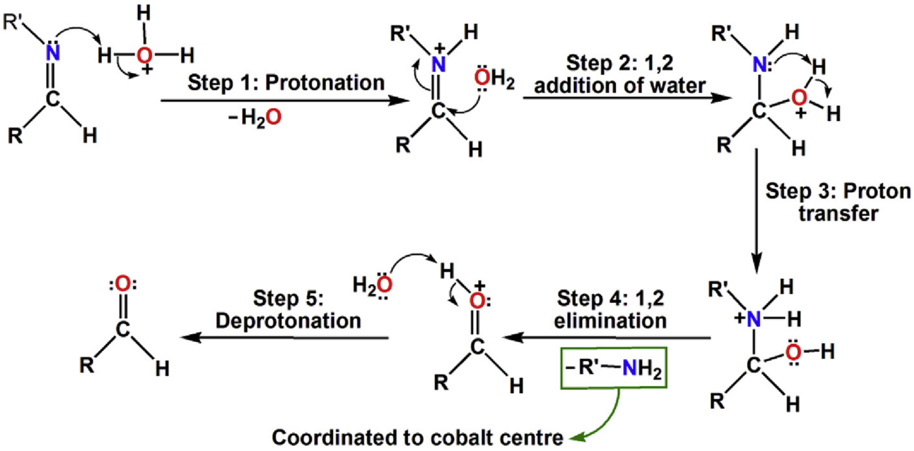

Scheme 2. Probable mechanistic pathway for *in situ* formation of amine ligand.

3.3. Theoretical calculations of solid state supramolecular interactions

The complex contains Br atoms in its structure that participates in a “non-directional” halogen bonding with the azide coligand, which is uncommon for halogen bonding. The theoretical study is devoted to analyse the energy associated to the halogen bonding interactions along with other more conventional interactions like hydrogen bonding and C—H$\cdots\pi$.

In Fig. 2, we represent a partial view of the X-ray packing of the complex where two infinite and anti-parallel 1D supramolecular chains are represented. The creation of these 1D assemblies is governed by the formation of $N_3\cdots$H—N interactions, represented as black dashed lines. Curiously, the supramolecular chains are connected by means of Br···N contacts among other weak interactions (*vide infra*) that are analysed below.

First of all, we have studied the energy associated with H-bonding interactions that governs the formation of the 1D supramolecular chain. We have computed a dimer retrieved from the infinite chain (Fig. 3a) and its formation energy is strong $\Delta E_1 = -28.4$ kcal/mol because of the anionic nature of the azide ligand and the enhanced acidity of the —NH_2 group (H-bond donor) due to its coordination to the metal centre. We have also computed the “non-covalent Interaction plot” (NCI plot) index in order to characterize the interactions in this dimer of the complex. The NCI plot is an intuitive visualization index that enables the identification of non-covalent interactions easily and efficiently. The NCI plot is convenient to analyse host—guest interactions since it clearly shows which molecular regions interact. The colour scheme is a red-yellow-green-blue scale with red (repulsive) and blue (attractive). Yellow and green surfaces correspond to weak repulsive and weak attractive interactions, respectively. The representation of the NCI plot is shown in Fig. 3b. As noted, the hydrogen bond is characterized by the presence of a small blue isosurface between the N—H and N_3^- groups. Quite interestingly, the NCI plot reveals the existence of a green and more extended isosurface between the azido ligand and the aromatic ring, thus suggesting the presence of an anion—π interaction, also indicated in Fig. 3a. Finally, there is also a weak interaction (green isosurface) between the other aromatic ring and the ethyl group of the aliphatic ligand, thus suggesting the participation of a C—H$\cdots\pi$ interaction that also contributes to the stabilization of the assembly. This analysis reveals a quite intricate combination of noncovalent bonds (the stronger is the H-bond as revealed by the color of the surface) that govern the formation of the 1D supramolecular assembly in the complex.

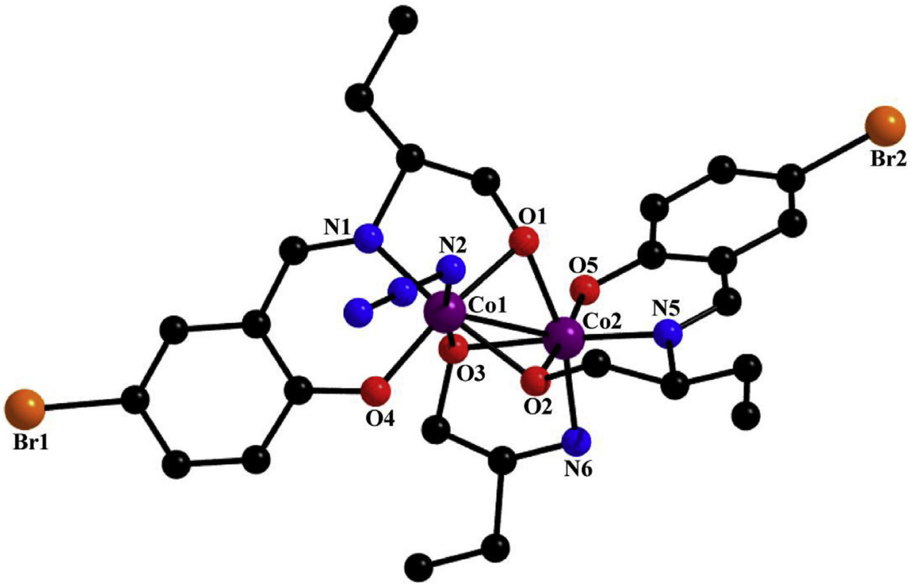

Fig. 1. Molecular structure of the complex with selective atom numbering scheme. Only the major component of the disorder has been shown. Hydrogen atoms and lattice water molecules have been omitted for clarity.

Table 2
Selected bond lengths (Å) of the titled complex.

Co(1)-O(1)	1.906(3)
Co(1)-O(2)	1.935(3)
Co(1)-O(3)	1.950(3)
Co(1)-O(4)	1.859(3)
Co(1)-N(1)	1.845(4)
Co(1)-N(2)	1.936(4)
Co(2)-O(1)	1.969(3)
Co(2)-O(2)	1.888(3)
Co(2)-O(3)	1.898(3)
Co(2)-O(5)	1.873(3)
Co(1)-N(5)	1.866(3)
Co(1)-N(6)	1.927(4)

Table 3
Selected bond angles (°) of the titled complex.

O(1)-Co(1)-O(2)	81.61(12)	O(1)-Co(2)-O(2)	81.16(12)
O(1)-Co(1)-O(3)	79.85(12)	O(1)-Co(2)-O(3)	79.55(12)
O(1)-Co(1)-O(4)	172.49(13)	O(1)-Co(2)-O(5)	94.99(12)
O(1)-Co(1)-N(1)	89.03(16)	O(1)-Co(2)-N(5)	98.09(15)
O(1)-Co(1)-N(2)	92.89(15)	O(1)-Co(2)-N(6)	165.62(13)
O(2)-Co(1)-O(3)	79.93(12)	O(2)-Co(2)-O(3)	82.44(12)
O(2)-Co(1)-O(4)	92.11(12)	O(2)-Co(2)-O(5)	175.31(12)
O(2)-Co(1)-N(1)	168.44(18)	O(2)-Co(2)-N(5)	87.21(14)
O(2)-Co(1)-N(2)	95.87(15)	O(2)-Co(2)-N(6)	91.93(13)
O(3)-Co(1)-O(4)	95.06(12)	O(3)-Co(2)-O(5)	94.27(12)
O(3)-Co(1)-N(1)	91.80(17)	O(3)-Co(2)-N(5)	169.61(15)
O(3)-Co(1)-N(2)	172.04(15)	O(3)-Co(2)-N(6)	87.08(13)
O(4)-Co(1)-N(1)	96.70(16)	O(5)-Co(2)-N(5)	96.02(14)
O(4)-Co(1)-N(2)	91.84(15)	O(5)-Co(2)-N(6)	91.23(13)
N(1)-Co(1)-N(2)	91.35(19)	N(5)-Co(2)-N(6)	94.13(15)

We have also computed the dimer retrieved from the X-ray structure where two symmetrically related Br···N interactions are formed and connect the 1D chain (Fig. 2). As can be observed in Fig. 4a, the directionality of the Br···N interaction is not the typical for a halogen bond, which is usually very linear. We have computed the interaction energy of this dimer, which is very large ($\Delta E_2 = -45.2$ kcal/mol) due to the participation of several interactions including C-H···π and C-H···N, as indicated in Fig. 3a. In an effort to estimate the contribution of the Br···N interactions to the binding energy of the dimer, we have computed a theoretical dimer where the Br atoms have been replaced by H-atoms (small arrows in Fig. 4b). As a result, the binding energy is slightly reduced to $\Delta E_3 = -43.3$ kcal/mol, thus indicating that the contribution of both Br···N interactions is very small (−1.9 kcal/mol). This small contribution is likely due to the directionality of the interaction, where the Br atom is pointing to the π-system of the azido ligand. Therefore, this weak interaction might be better defined as a Br···π halogen bond. We have also computed the NCI plot index in order to characterize the halogen bonding interaction in the dimer of the complex (Fig. 4c). The halogen bond is characterized by a small green isosurface that is located between the Br and one N atom of the azido ligand. Moreover, an additional green isosurfaces are located between the aromatic H atoms and two N atoms of the azido ligand, also contributing to the stabilization of the dimer. In addition, several green isosurfaces are located between both dimers, thus revealing the existence of several van der Waals contacts (including C—H···π interactions) that explain the large binding energy obtained for this dimer.

3.4. Hirshfeld surface analysis

In solid state, crystal structure of a complex can be determined by a combination of several significant intermolecular and intramolecular interactions, and hence all these interactions should be taken into account. Hirshfeld surface analysis helps us to visualize and investigate these important interactions. Visualization and investigation of these major interactions using Hirshfeld surface-based tools symbolize a crucial progress in enabling supramolecular chemists and crystal engineers to gain insight into crystal packing. The Hirshfeld surfaces of the synthesized complex mapped over none, d_i, d_e, d_{norm}, shape index and curvedness shown in Fig. 5. The surfaces are shown as transparent so that the molecular moieties around which Hirshfeld surfaces are calculated could be visualized. Generally, Hirshfeld surface and properties defined by it emphasize a whole-of-molecule approach to understanding intermolecular interactions, they can also be used in conjunction with a more direct atom···atom based approach to gain a fuller

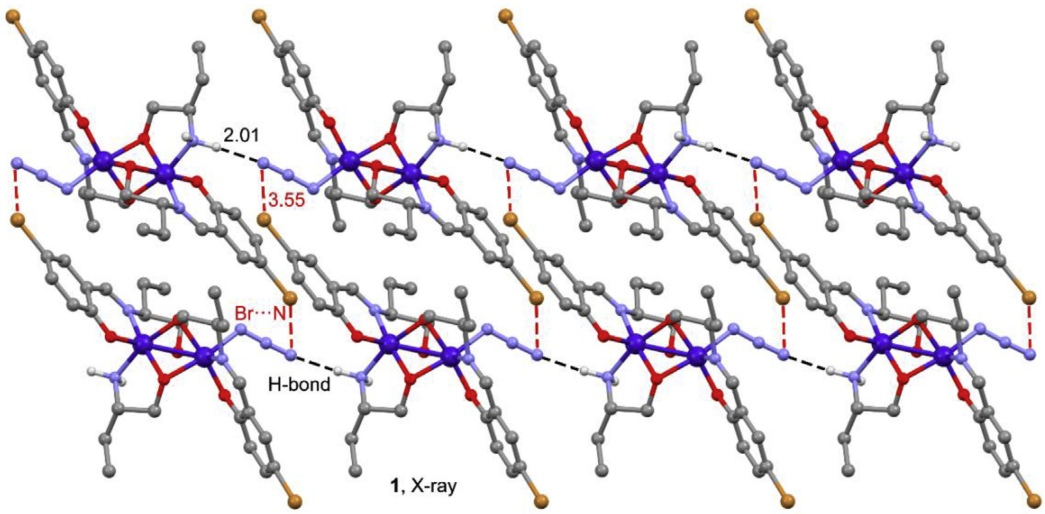

Fig. 2. 1D supramolecular chain observed in the X-ray solid state structure of the complex. Only the hydrogens participating in hydrogen bonds have been shown for clarity.

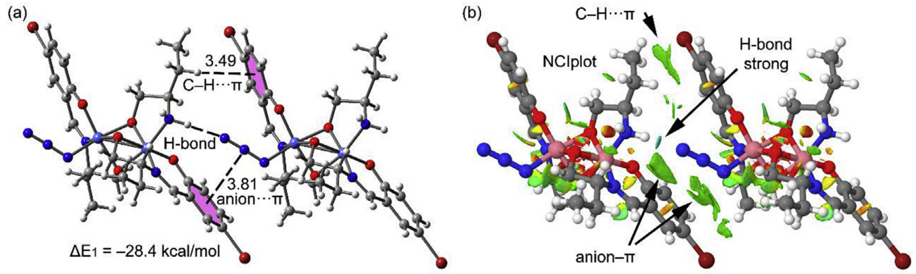

Fig. 3. (a) Dimer extracted from the 1D supramolecular chain observed in the X-ray solid state structure of the complex and its interaction energy. (b) NCI surface of the dimer of the complex, extracted from the 1D supramolecular chain. The gradient cut-off is $s = 0.35$ au, and the color scale is $-0.04 < \rho < 0.04$ au. (For interpretation of the references to color in this figure legend, the reader is referred to the Web version of this article.)

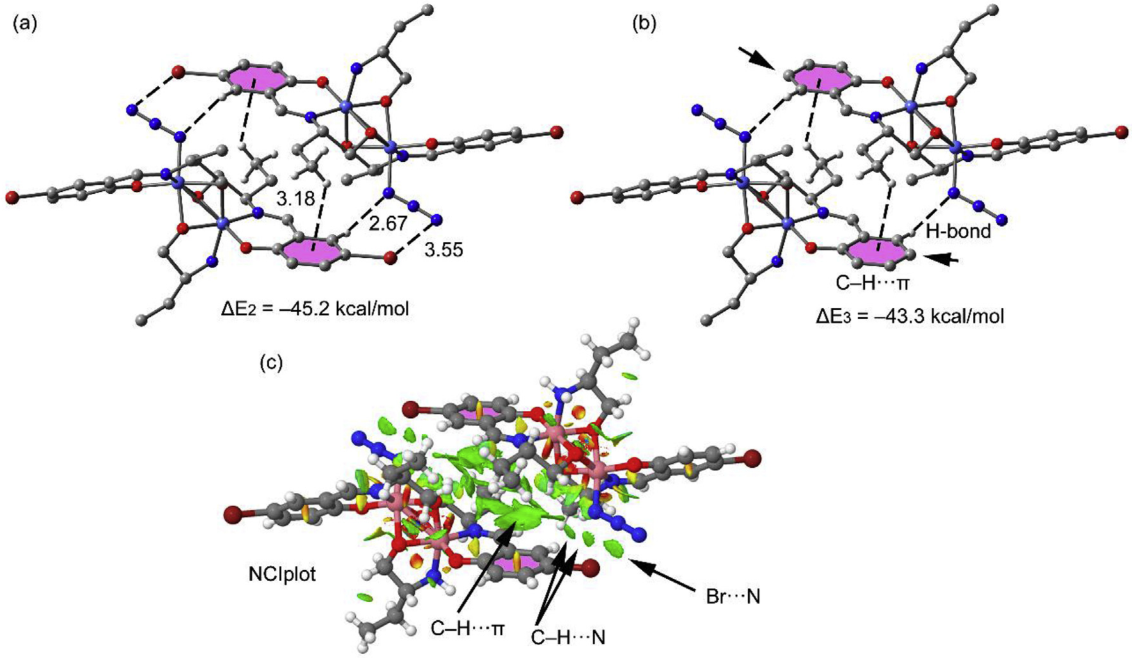

Fig. 4. (a) Dimer retrieved from the crystal structure of the complex. Distances in Å. (b) Model without any Br atoms, which has been replaced by H-atoms (c) NCI surface of the dimer of complex. The gradient cut-off is $s = 0.35$ au, and the color scale is $-0.04 < \rho < 0.04$ au. (For interpretation of the references to color in this figure legend, the reader is referred to the Web version of this article.)

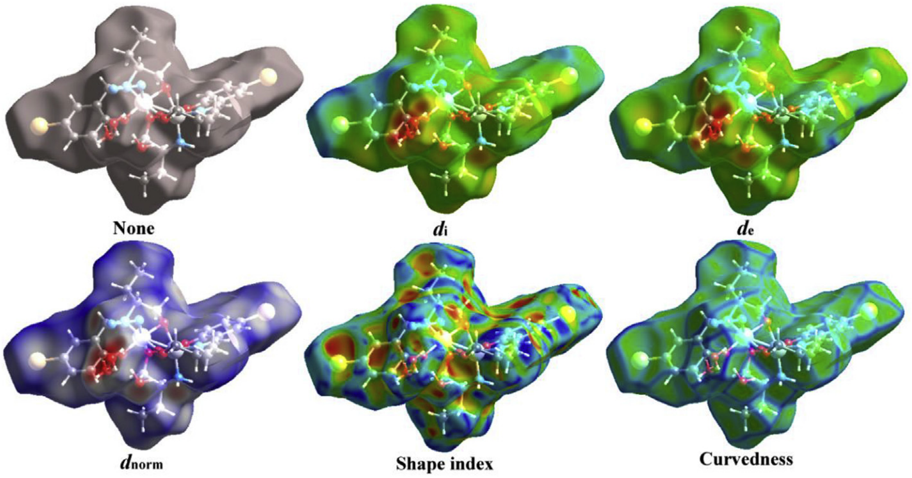

Fig. 5. Hirshfeld surfaces of the complex mapped with none, d_i, d_e, d_{norm}, shape index and curvedness.

appreciation of the important interactions in a molecular crystal. The dominant interactions of the complex are H···H, C···H/H···C, N···H/H···N, O···H/H···O and Br···H/H···Br. Red spots on the d_{norm} surface (Fig. 5) indicate that these interactions are dominant. Additionally, the two dimensional fingerprint plots (Fig. 6) exemplify various inter-molecular interaction patterns associated with the complex and their relative contributions in percentage scale. In the two dimensional fingerprint plots inter-molecular interactions become visible as distinct spikes. Complementary regions are visible in the two dimensional fingerprint plots where one molecule act as donor ($de > di$) and the other as an acceptor ($de < di$). Fingerprint plots can also be exploited to highlight the selected atoms pair close contacts. This exploitation permits separation of contributions from different interaction types, which overlap in the whole fingerprint plots [63].

3.5. Spectral and magnetic characterization

The IR and electronic spectra of the synthesized complex are in excellent agreement with its crystal structure. Some of the

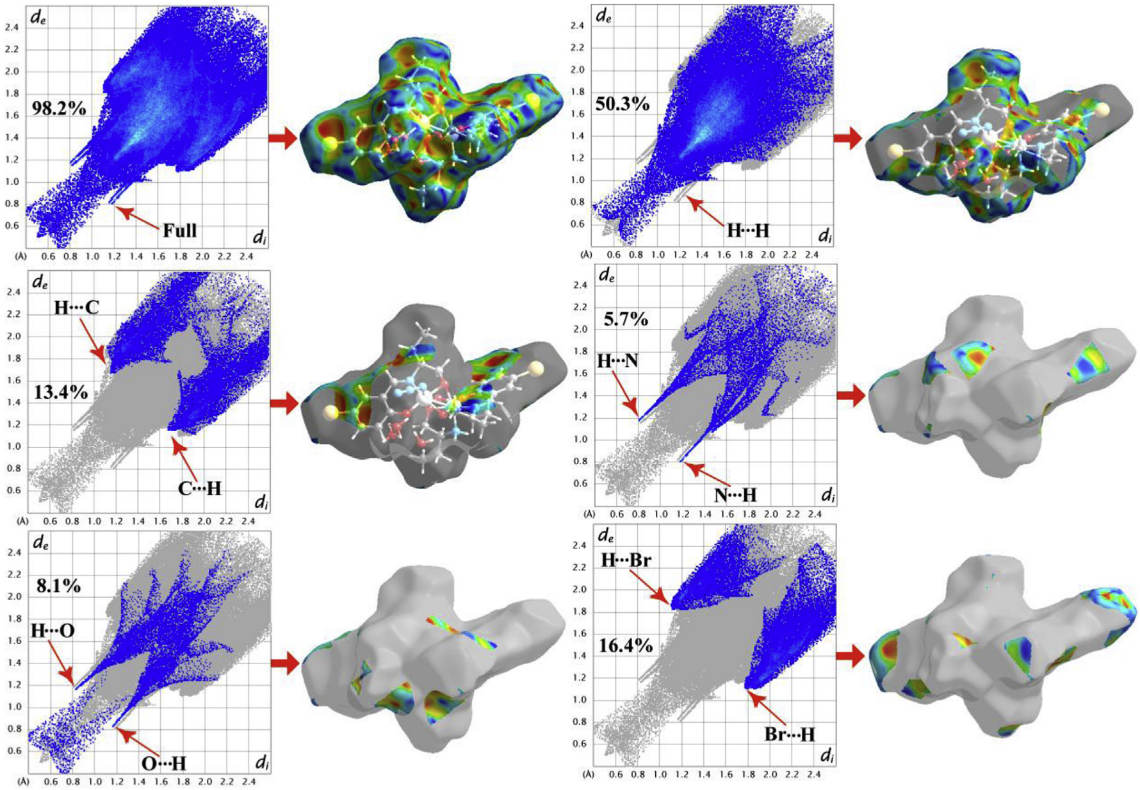

Fig. 6. Two dimensional fingerprint plots of the complex: Full and resolved into H···H, C···H/H···C, O···H/H···O, N···H/H···N and Br···H/H···Br contacts showing the percentages of contacts contributed to the total Hirshfeld Surface area of the complex. Surfaces in the right hand columns highlight the relevant surface patches associated with the specific contacts in the total Hirshfeld Surface area of the complex.

extremely informative infrared and electronic absorptions which assist in the structural characterization of the complex are gathered in the Experimental section. In IR spectrum of the complex, distinct bands due to the azomethine (C=N) group at 1591 cm^{-1} and 1631 cm^{-1} are customarily noticed [64–66]. A strong absorption band in IR spectrum of the complex at 2021 cm^{-1} indicates the presence of terminal azide [67,68]. A moderately strong band at 3134 cm^{-1} is observed in IR spectrum of the complex, which may be ascribed to the N–H stretching vibration [26,27]. Broad bands in the range of 2880–2962 cm^{-1} due to alkyl C-H stretching vibrations are routinely noticed in IR spectrum of the complex [69,70]. A broad band centered at 3402 cm^{-1} is observed in IR spectrum of the complex due to O-H stretching of the water molecule, which is involved in hydrogen bonding [71,72].

The electronic spectrum of the complex in DMF medium consists of four most fundamental bands around 264 nm, 315 nm, 410 nm and 540 nm. An octahedral cobalt(III) complex, in presence of strong field ligand (like Schiff base) is expected to have two d-d transitions, $^1T_{1g} \leftarrow {}^1A_{1g}$ and $^1T_{2g} \leftarrow {}^1A_{1g}$ in the visible region along with higher energy charge transfer transitions. In present case, the electronic spectrum of synthesized complex shows broad absorption bands around 410 nm and 540 nm, corresponding to these two spin allowed d-d transitions, as was also observed in similar complexes [73,74]. High energy absorption bands around 264 nm and 316 nm may be attributed to the ligand to metal charge transfer transitions and intra-ligand $\pi \rightarrow \pi^*/n \rightarrow \pi^*$ transitions [75–77].

Magnetic susceptibility measurement at room temperature confirms that the complex is diamagnetic in nature, as expected for low spin octahedral cobalt(III) complexes [20,22,24,26].

3.6. Phosphate ester bond cleavage study

The complex was utilized as catalyst for hydrolysis of 4-NPP. The catalytic activity was performed in aqueous DMF (98% DMF, v/v) medium because of very good solubility of the complex, substrate and their products. The efficiency of P-O bond cleavage of the complex was screened completely by monitoring the spectral change in the wavelength scan (300-500 nm) of a mixture solution for 2 h where complex to substrate ratio is maintained around 1:100 stoichiometrically (Fig. 7). The electronically silent substrate 4-NPP leads to band maxima around 425 nm characteristic of 4-nitrophenolate ion owing to the hydrolytic action of the complex. The resulting solutions were also monitored spectrophotometrically after 48 h which show the formation of 4-nitrophenolate as the sole product with no further increase of band maxima. These consequences undoubtedly indicate that the complex is active towards phosphatase mimicking activity. A blank experiment without any catalyst for the hydrolysis of 4-NPP was also carried out under identical conditions and in this case, no significant growth of the absorption bands around 425 nm was observed. The complete kinetic investigations were performed to realize the extent of the catalytic efficiency.

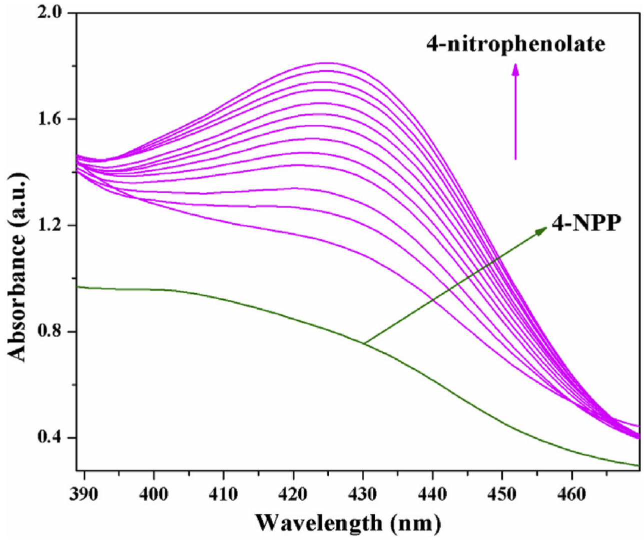

Fig. 7. Time resolved wavelength scan for the hydrolysis of 4-NPP in absence and presence of the complex in aqueous DMF (98% DMF, v/v) at an interval of 3 min.

3.7. Complete kinetic investigation through a number of enzyme kinetic plots

The Michaelis-Menten model is the simplest and best-known approach to evaluate the kinetic parameters of biochemical reactions involving a single substrate. However, Lineweaver–Burk, Hanes–Woolf and Eadie–Hofstee equations, which can be obtained through modification of Michaelis–Menten equation, may also be utilized to treat this type of biochemical reactions. All these equations are used to evaluate various kinetic parameters for phosphatase mimicking activity of the complex. In enzyme kinetics, turnover number (also termed as k_{cat}) is defined as the maximum number of chemical conversions of substrate molecules per unit time that a single catalytic site will execute for a specific enzyme concentration. The turnover number (k_{cat}) is calculated by dividing the V_{max} by the concentration of the catalyst used. The specificity constant (also termed as k_{cat}/K_M ratio) is a measure of how efficiently a catalyst converts substrates into products. This ratio is a useful index for measuring the substrate specificity of catalyst. A comparison of specificity constants can also be used as a measure of the preference of an enzyme for different substrates. The higher the specificity constant, the more the enzyme prefers that substrate. Fig. 8 represents the Michaelis–Menten, Lineweaver–Burk, Hanes–Woolf and Eadie–Hofstee plots of the complex for catalytic conversation of 4-nitrophenylphosphate to 4-nitrophenolate. All kinetic parameters for phosphatase mimicking activity of the complex is gathered in Table 4. The k_{cat} value suggest that the complex is very much effective towards catalytic conversation of 4-nitrophenylphosphate to 4-nitrophenolate.

3.8. Mechanistic pathway of phosphatase mimicking activity

It is evident from the reaction kinetics that the complex could be acts as efficient catalyst for hydrolysis of 4-nitrophenylphosphate at 25 °C. A number of factors may influence the catalytic activity, such as the variable oxidation state of the metal, coordination geometry around the metal centre, metal-metal distance, ligand flexibility, exogenous bridging ligand etc [33,78–80]. The catalytic activity depends on the interaction between substrate and catalyst. In several previous reports where mechanistic considerations of these types of catalytic P-O bond cleavage investigations are presented, it is established that the hydrolysis proceeds through a stable catalyst-substrate intermediate [29,32,81,82]. It is worthy to mention here that the mechanistic pathway may proceed through a multistep sequence and catalytic cycle initiates with the nucleophilic attack on the phosphorus atom of the substrate, leading to the cleavage of the P-O bond, as suggested by M. Toscano *et al* [83]. Based on these previous reports, we can assume that the reaction mechanism proceeds through at least one stable catalyst-substrate intermediate. Catalytic aerobic oxidation of 4-nitrophenylphosphate is depicted in Scheme 3.

In order to get an insight into the nature of probable catalyst-substrate intermediate, the ESI-MS positive spectrum of a 1: 40

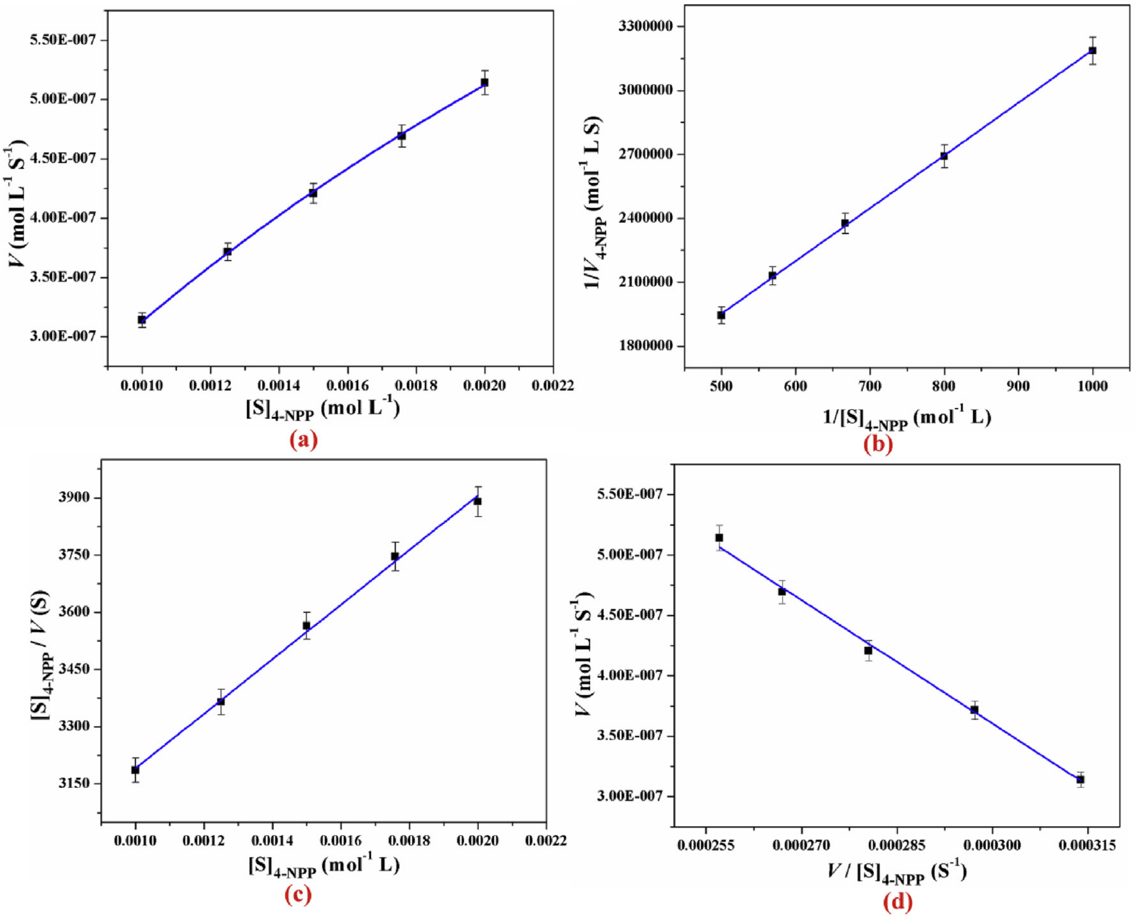

Fig. 8. Michaelis–Menten plot (a), Lineweaver–Burk plot (b), Hanes–Woolf plot (c) and Eadie–Hofstee plot (d) of the complex for catalytic conversation of 4-nitrophenylphosphate to 4-nitrophenolate.

Table 4
Kinetic parameters of the complex for phosphatase mimicking activity using various enzyme kinetic plots at 25 °C in DMF-water medium.

Enzyme kinetic plots	$V_{max} \pm$ SE (M S^{-1})	$K_M \pm$ SE (M)	$k_{cat} \pm$ SE (S^{-1})	$k_{cat}/K_M \pm$ SE (S^{-1} M^{-1})
Michaelis-Menten Plot	(1.411 ± 0.004) x 10^{-6}	(35.100 ± 0.001) x 10^{-4}	(1.411 ± 0.004) x 10^{-1}	(0.402 ± 0.004) x 10^{+2}
Lineweaver-Burk plot	(1.396 ± 0.018) x 10^{-6}	(34.542 ± 0.003) x 10^{-4}	(1.396 ± 0.018) x 10^{-1}	(0.404 ± 0.004) x 10^{+2}
Hanes-Woolf plot	(1.396 ± 0.012) x 10^{-6}	(34.542 ± 0.002) x 10^{-4}	(1.396 ± 0.012) x 10^{-1}	(0.404 ± 0.003) x 10^{+2}
Eadie-Hofstee plot	(1.382 ± 0.006) x 10^{-6}	(34.100 ± 0.001) x 10^{-4}	(1.382 ± 0.006) x 10^{-1}	(0.401 ± 0.002) x 10^{+2}

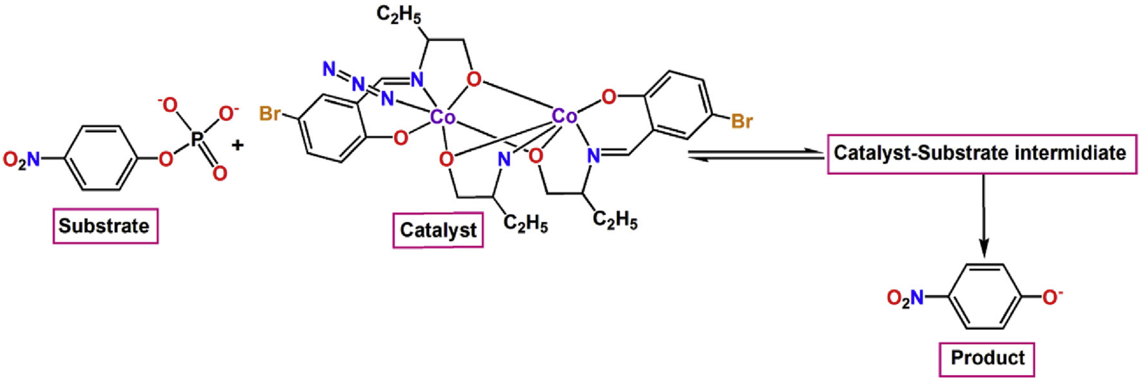

Scheme 3. Catalytic aerobic oxidation of 4-nitrophenylphosphate to 4-nitrophenolate.

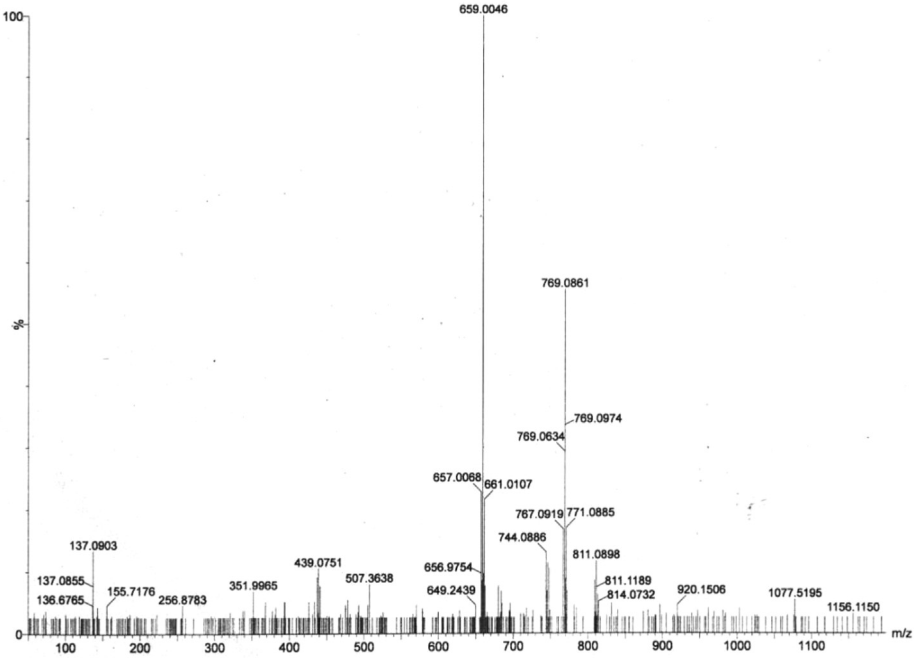

Fig. 9. Electrospray ionization mass spectrum (ESI-MS positive) of 1: 40 mixture of the complex and 4-nitrophenylphosphate in DMF medium.

mixture of the complex and 4-nitrophenylphosphate in DMF was recorded after 2 min of mixing, and the related spectrum is depicted in Fig. 9. ESI-MS positive spectrum of the complex is also recorded just to achieve a correlation and to determine the stability of the catalyst in reaction medium (Fig. 10). The peak at $m/z = 769.0861$ corresponds to the formation of catalyst-substrate intermediate, $[Co(L^1)(L^2)(4\text{-}NPP)(DMF)(Na)(K)]^+$. The peak around m/z ~659 is indicative of a fragment of the catalyst, $[Co_2(L^1)_2]^+$, corresponding to the loss of amine moiety and azide. Here also it is worth mentioning that during the formation of this fragment, one Co^{III} is reduced to Co^{II}. Such kind of reduction is observed in ESI-Ms mass spectra of transition metal complexes [84-86].

3.9. Photocatalytic degradation of methylene blue

For detail investigation of photocatalytic activity of the complex, methylene blue (MB) is selected as models of dye contaminant. Interestingly, the synthesized complex displays the photocatalytic activities under visible light irradiation. As illustrated in Fig. 11, the absorption peak of MB decreased distinctly with the irradiation time increasing from 0 to 90 min in the presence of the complex, which clearly indicates the photocatalytic degradation of MB. It is evident that the intensity of the characteristic absorption peak of MB (~600 nm) decreased with the increase of irradiation time in the degradation process. Additionally, the photocatalytic degradation efficiency of the complex is defined as C_t/C_0, where C_t and C_0 symbolize the remnant and initial concentration of methylene blue, respectively. The changes in the C_t/C_0 plot of MB solution versus irradiation time are shown in Fig. 12. The calculation of experimental results shows that the complex is able to degrade ca. 55% of

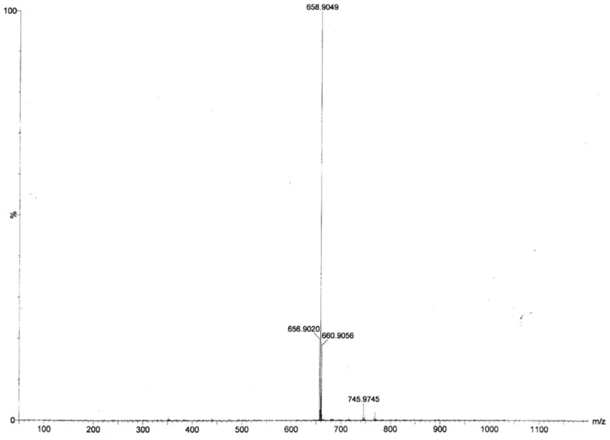

Fig. 10. Electrospray ionization mass spectrum (ESI-MS positive) of the complex in DMF medium.

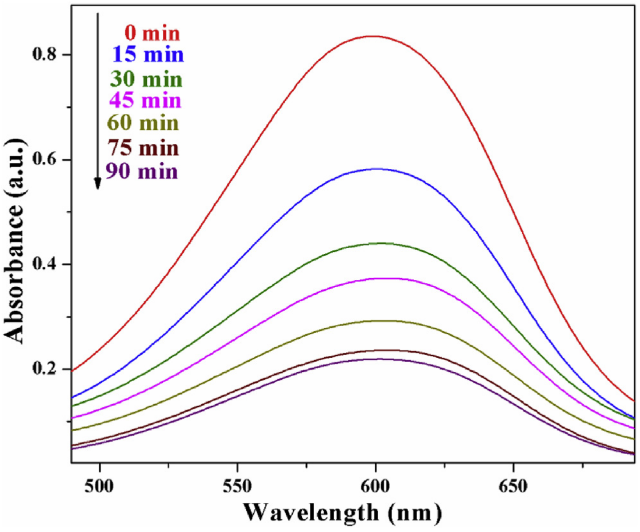

Fig. 11. Absorption spectra of the MB solution during the decomposition reaction under visible light irradiation in the presence of the complex.

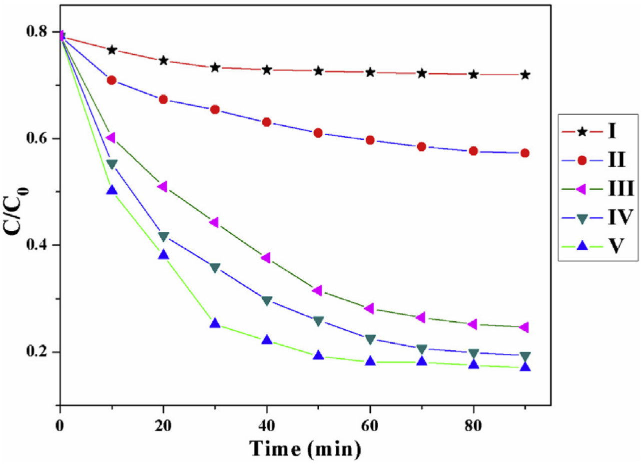

Fig. 12. Photocatalytic decomposition of MB solution under visible light irradiation without any complex (curve I), with the use of cobalt(II) acetate tetrahydrate (curve II) and with different amounts of complex (curve III, IV and V with 8, 10 and 12 mg complex, respectively) under identical environment.

MB after 90 min of irradiation using only 8 mg of the complex (curve III of Fig. 12). Use of 10 and 12 mg of the complex, the ratio of the degradation reaches about 60 and 82%, respectively (curve IV and V of Fig. 12).

To confirm the photocatalytic activity of the complex, a similar experiment without any catalyst under identical environment have been performed, which showed only very little decomposition of MB. The photocatalytic activity of cobalt(II) acetate tetrahydrate has also been studied to MB under identical condition, which showed that the rate of degradation was still very slow (less than 20%).

A reasonable mechanistic pathway for the photocatalytic degradation of organic dye is given in Scheme 4. As shown in the several previously reported articles [30–32], the optical band gap (E_g) is the most important factor affecting the speed of the photocatalytic degradation of methylene blue. The band gap (E_g) may be defined as the intersection point between the energy axis and the line extrapolated from the linear portion of the adsorption edge. It is easily understandable that at initial step of photocatalytic cycle is the promotion of electrons (e^-) from valence band (VB) to conduction band (CB) upon irradiation of visible light. Due to this excitation phenomenon equal amount of holes (h^+) is created in VB. It is a well known fact that holes (h^+) can act as powerful oxidants and electrons (e^-) can act as powerful reductants. So, effective degradation of MB can easily be happen in presence of holes. On the other hand, the adsorption of molecular oxygen (O_2) or the hydroxyl ion (OH^-) on the surface of the complex and eventually it gets converted to hydroxyl radical ($\dot{O}H$) which is also responsible for effective degradation of MB.

In order to verify whether the complex is capable of maintaining its structural integrity after photocatalytic process, IR spectrum of the complex was recorded before and after photocatalytic reaction. The IR spectrum of the complex after photocatalytic reaction is in excellent agreement with the IR spectrum of pure complex, confirming the structural integrity of the complex after photocatalytic degradation of MB. Alternatively, we can say that the complex is chemically intact during the photocatalytic reaction. Fig. 13 illustrates IR spectrum of the complex before and after the photodegradation process.

4. Concluding remarks

In a nutshell, a dinuclear alkoxo bridged cobalt(III) Schiff base complex has been synthesized and structurally characterized. The complex is found to exhibit several significant non-covalent interactions i.e. halogen and hydrogen bonding in the solid state. Analysis of energies associated to these interactions has been conducted using DFT calculations, and further corroborated with

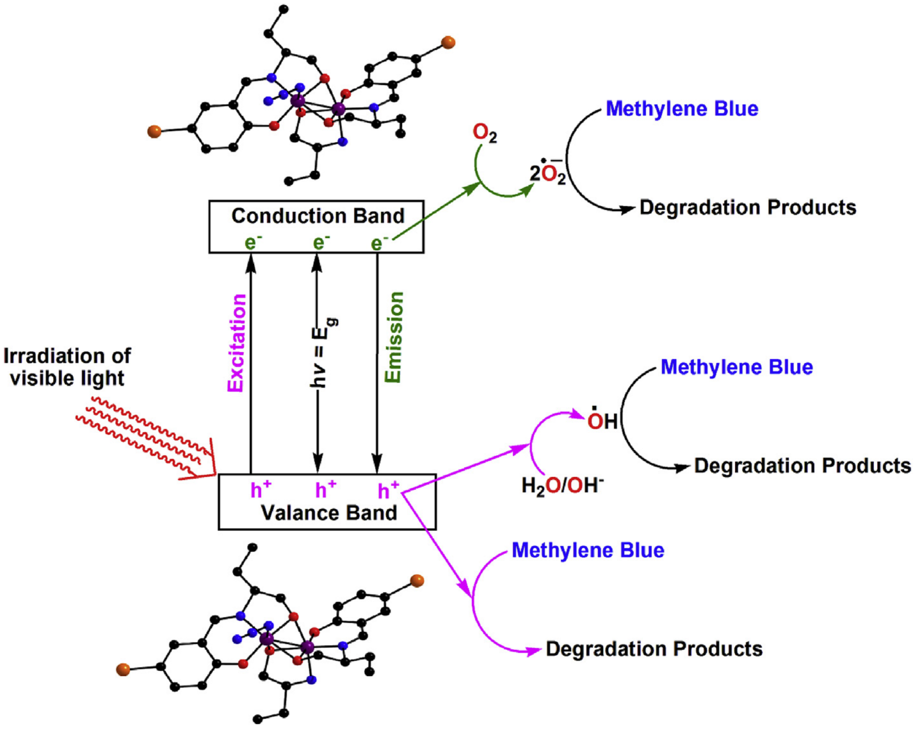

Scheme 4. Probable mechanistic pathway for the photocatalytic degradation of methylene blue.

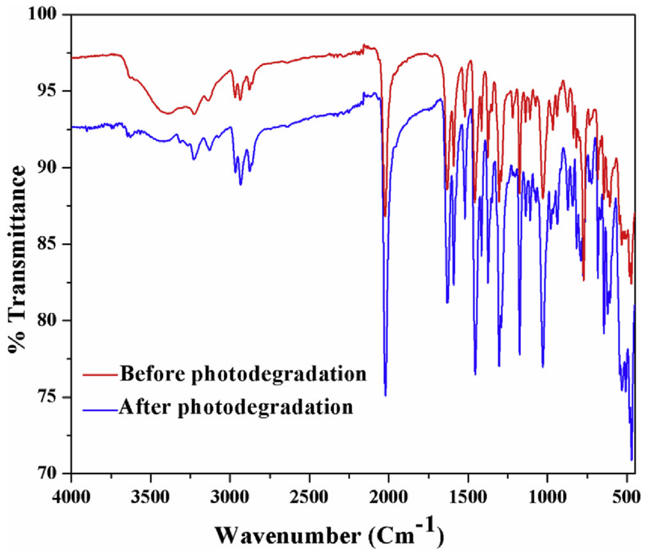

Fig. 13. IR spectrum of the complex before (red) and after (blue) the photodegradation process (blue). (For interpretation of the references to color in this figure legend, the reader is referred to the Web version of this article.)

NCI plot index computational tool. It presents an intricate combination of interactions including relevant C-H$\cdots\pi$ and anion$\cdots\pi$ that assist to construction of the solid state architecture of the complex. The complex is capable of showing appreciable phosphatase activity ($k_{cat} = \sim 0.14\ s^{-1}$) with 4-NPP substrate. In addition, the complex presents significantly impressive photocatalytic activity for the decomposition of MB under irradiation of visible light. Work is in progress to prepare other new cluster-based coordination complexes with improved photocatalytic activities for the degradation of other organic dyes. In view of these merits, we anticipate that the titled complex would open up a new direction for the development of multifunctional molecular entities for bioanalytical and biomimetic applications.

Acknowledgements

K.G. expresses his gratitude to UGC, India, for awarding a Senior Research Fellowship. AF thanks the MINECO/AEI from Spain for a “Juan de la Cierva” contract. We thank the MINECO/AEI from Spain for financial support (project number CTQ2017-85821-R, FEDER funds). We are grateful to the CTI (UIB) for free allocation of computer time.

Appendix A. Supplementary data

CCDC 1876149 contains the supplementary crystallographic data of the complex. This data can be obtained free of charge via http://www.ccdc.cam.ac.uk/conts/retrieving.html, or from the Cambridge Crystallographic Data Centre, 12 Union Road, Cambridge CB2 1EZ, UK; fax: (+44) 1223-336-033; or e-mail: deposit@ccdc.cam.ac.uk.

Supplementary data to this article can be found online at https://doi.org/10.1016/j.jorganchem.2019.01.006.

References

[1] X. Ma, E.A. Suturina, S. De, P. Négrier, M. Rouziéres, R. Clérac, P. Dechambenoit, Angew. Chem. Int. Ed. 57 (2018) 7841–7845.
[2] J. Long, F. Habib, P.-H. Lin, I. Korobkov, G. Enright, L. Ungur, W. Wernsdorfer, L.F. Chibotaru, M. Murugesu, J. Am. Chem. Soc. 133 (2011) 5319–5328.
[3] S. Fortier, J.J.L. Roy, C.-H. Chen, V. Vieru, M. Murugesu, L.F. Chibotaru, D.J. Mindiola, K.G. Caulton, J. Am. Chem. Soc. 135 (2013) 14670–14678.
[4] L.K. Thompson, S.K. Mandal, S.S. Tandon, J.N. Bridson, M.K. Park, Inorg. Chem. 35 (1996) 3117–3125.
[5] E. Ruiz, J. Cano, S. Alvarez, P. Alemany, J. Am. Chem. Soc. 120 (1998) 11122–11129.
[6] P. Román, C. Guzmán-Miralles, A. Luque, J.I. Beitia, J. Cano, F. Lloret, M. Julve, S. Alvarez, Inorg. Chem. 35 (1996) 3741–3751.
[7] L.J. Daumann, P. Comba, J.A. Larrabee, G. Schenk, R. Stranger, G. Cavigliasso, L.R. Gahan, Inorg. Chem. 52 (2013) 2029–2043.
[8] A. Banerjee, A. Guha, J. Adhikary, A. Khan, K. Manna, S. Dey, E. Zangrando, D. Das, Polyhedron 60 (2013) 102–109.
[9] M.M. Ibrahim, N. Shimomura, K. Ichikawa, M. Shiro, Inorg. Chim. Acta. 313 (2001) 125–136.
[10] A. Neves, M. Lanznaster, A.J. Bortoluzzi, R.A. Peralta, A. Casellato, E.E. Castellano, P. Herrald, M.J. Riley, G. Schenk, J. Am. Chem. Soc. 129 (2007) 7486–7487.
[11] T. Koike, E. Kimura, J. Am. Chem. Soc. 113 (1991) 8935–8941.
[12] T. Robinson, G. McMullan, R. Marchant, P. Nigam, Bioresour. Technol. 77 (2001) 247–255.
[13] T.H. Pearson, Oceanogr. Mar. Biol. Annu. Rev. 16 (1978) 229–311.
[14] H. Wang, C. Wang, W. Wu, Z. Mo, Z. Wang, Chemosphere 50 (2003) 557–562.
[15] L. Liu, J. Ding, C. Huang, M. Li, H. Hou, Y. Fan, Cryst. Growth Des. 14 (2014) 3035–3043.
[16] S.P. Buthelezi, A.O. Olaniran, B. Pillay, Molecules 17 (2012) 14260–14274.
[17] A. Patsoura, D.I. Kondarides, X.E. Verykios, Catal. Today 124 (2007) 94–102.
[18] D. Chatterjee, S. Dasgupta, J. Photochem, C. Photobiol, Photochem. Rev. 6 (2005) 186–205.
[19] L. Gomathi Devi, R. Kavitha, Appl. Catal. B Environ. 140–141 (2013) 559–587.
[20] K. Ghosh, S. Roy, A. Ghosh, A. Banerjee, A. Bauzá, A. Frontera, S. Chattopadhyay, Polyhedron 112 (2016) 6–17.
[21] T. Basak, A. Bhattacharyya, M. Das, K. Harms, A. Bauzá, A. Frontera, S. Chattopadhyay, ChemistrySelect 2 (2017) 6286–6295.
[22] K. Ghosh, K. Harms, S. Chattopadhyay, Polyhedron 123 (2017) 162–175.
[23] S. Roy, A. Bhattacharyya, S. Herrero, R. González-Prieto, A. Frontera, S. Chattopadhyay, ChemistrySelect 2 (2017) 6535–6543.
[24] K. Ghosh, K. Harms, S. Chattopadhyay, ChemistrySelect 2 (2017) 8207–8220.
[25] S. Roy, M.G.B. Drew, S. Chattopadhyay, Polyhedron 150 (2018) 28–34.
[26] K. Ghosh, A. Banerjee, A. Bauzá, A. Frontera, S. Chattopadhyay, RSC Adv. 8 (2018) 28216–28237.
[27] T. Basak, K. Ghosh, S. Chattopadhyay, Polyhedron 146 (2018) 81–92.
[28] K. Ghosh, M.G.B. Drew, S. Chattopadhyay, Inorg. Chim. Acta. 482 (2018) 23–33.
[29] T. Basak, M.G.B. Drew, S. Chattopadhyay, Inorg. Chem. Commun. 98 (2018) 92–98.
[30] S. Roy, K. Harms, A. Bauzá, A. Frontera, S. Chattopadhyay, Polyhedron 121 (2017) 199–205.
[31] S. Roy, K. Harms, S. Chattopadhyay, Polyhedron 127 (2017) 471–477.
[32] T. Basak, A. Bhattacharyya, K. Harms, S. Chattopadhyay, Polyhedron 157 (2019) 449–457.
[33] R. Sanyal, X. Zhang, P. Chakraborty, F.A. Mautner, C. Zhao, D. Das, RSC Adv. 6 (2016) 73534–73546.
[34] S. Mandal, Y. Sikdar, D.K. Maiti, R. Sanyal, D. Das, A. Mukherjee, S.K. Mandal, J.K. Biswas, A. Bauzá, A. Frontera, S. Goswami, J. Photochem, A. Photobiol, Chemistry 334 (2017) 86–100.
[35] J.S. Seo, N.-D. Sung, R.C. Hynes, J. Chin, Inorg. Chem. 35 (1996) 7472–7473.
[36] D.R. Jones, L.F. Lindoy, A.M. Sargeson, J. Am. Chem. Soc. 106 (1984) 7807–7819.
[37] N.H. Williams, A.-M. Lebuis, J. Chin, J. Am. Chem. Soc. 121 (1999) 3341–3348.
[38] T. Wen, D.-X. Zhang, J. Zhang, Inorg. Chem. 52 (2013) 12–14.
[39] W. Meng, Z. Xu, J. Ding, D. Wu, X. Han, H. Hou, Y. Fan, Cryst. Growth Des. 14 (2014) 730–738.
[40] W. Cui, W. An, L. Liu, J. Hu, Y. Liang, J. Hazard Mater. 280 (2014) 417–427.
[41] X-Area LANA, STOE & Cie GmbH, Darmstadt, Germany, 2016.
[42] G.M. Sheldrick, Acta Crystallogr. A71 (2015) 3–8.
[43] G.M. Sheldrick, Acta Crystallogr. C71 (2015) 3–8.
[44] D. Kratzert, J.J. Holstein, I. Krossing, J. Appl. Crystallogr. 48 (2015) 933–938.
[45] G.M. Sheldrick, Acta Crystallogr. A64 (2008) 112–122.
[46] G.M. Sheldrick, SADABS: Software for Empirical Absorption Correction, University of Göttingen, Institute fur Anorganische Chemieder Universitat, Gottingen, Germany, 1999-2003.
[47] M.J. Frisch, G.W. Trucks, H.B. Schlegel, G.E. Scuseria, M.A. Robb, J.R. Cheeseman, G. Scalmani, V. Barone, B. Mennucci, G.A. Petersson, H. Nakatsuji, M. Caricato, X. Li, H.P. Hratchian, A.F. Izmaylov, J. Bloino, G. Zheng, J.L. Sonnenberg, M. Hada, M. Ehara, K. Toyota, R. Fukuda, J. Hasegawa, M. Ishida, T. Nakajima, Y. Honda, O. Kitao, H. Nakai, T. Vreven, J.A. Montgomery Jr., J.E. Peralta, F. Ogliaro, M. Bearpark, J.J. Heyd, E. Brothers, K.N. Kudin, V.N. Staroverov, R. Kobayashi, J. Normand, K. Raghavachari, A. Rendell, J.C. Burant, S.S. Iyengar, J. Tomasi, M. Cossi, N. Rega, J.M. Millam, M. Klene, J.E. Knox, J.B. Cross, V. Bakken, C. Adamo, J. Jaramillo, R. Gomperts, R.E. Stratmann, O. Yazyev, A.J. Austin, R. Cammi, C. Pomelli, J.W. Ochterski, R.L. Martin, K. Morokuma, V.G. Zakrzewski, G.A. Voth, P. Salvador, J.J. Dannenberg, S. Dapprich, A.D. Daniels, Ö. Farkas, J.B. Foresman, J.V. Ortiz, J. Cioslowski, D.J. Fox, Gaussian 09, Gaussian, Inc., Wallingford CT, 2009.
[48] S. Grimme, J. Antony, S. Ehrlich, H. Krieg, J. Chem. Phys. 132 (2010) 154104.
[49] S.F. Boys, F. Bernardi, Mol. Phys. 19 (1970) 553–566.

[50] J. Contreras-García, E.R. Johnson, S. Keinan, R. Chaudret, J.-P. Piquemal, D.N. Beratan, W. Yang, J. Chem. Theor. Comput. 7 (2011) 625–632.
[51] M.A. Spackman, D. Jayatilaka, CrystEngComm 11 (2009) 19–32.
[52] F.L. Hirshfeld, Theor. Chim. Acta 44 (1977) 129–138.
[53] H.F. Clausen, M.S. Chevallier, M.A. Spackman, B.B. Iversen, New J. Chem. 34 (2010) 193–199.
[54] F.H. Allen, O. Kennard, D.G. Watson, L. Brammer, A.G. Orpen, R.J. Taylor, J. Chem. Soc., Perkin Trans. 2 (1987) S1–S19.
[55] K. Ghosh, A. Banerjee, S. Roy, A. Bauzá, A. Frontera, S. Chattopadhyay, Polyhedron 112 (2016) 86–95.
[56] N. Sarkar, M.G.B. Drew, K. Harms, A. Bauzá, A. Frontera, S. Chattopadhyay, CrystEngComm 20 (2018) 1077–1086.
[57] A.L. Rohl, M. Moret, W. Kaminsky, K. Claborn, J.J. McKinnon, B. Kahr, Cryst. Growth Des. 8 (2008) 4517–4525.
[58] A. Parkin, G. Barr, W. Dong, C.J. Gilmore, D. Jayatilaka, J.J. McKinnon, M.A. Spackman, C.C. Wilson, CrystEngComm 9 (2007) 648–652.
[59] M.A. Spackman, J.J. McKinnon, CrystEngComm 4 (2002) 378–392.
[60] S.K. Wolff, D.J. Grimwood, J.J. McKinnon, D. Jayatilaka, M.A. Spackman, Crystal Explorer 2.0, University of Western Australia, Perth, Australia, 2007. http://hirshfeldsurfacenet.blogspot.com/.
[61] D. Cremer, J.A. Pople, J. Am. Chem. Soc. 97 (1975) 1354–1358.
[62] A.D. Hill, P.J. Reilly, J. Chem. Inf. Model. 47 (2007) 1031–1035.
[63] M.A. Spackman, P.G. Byrom, Chem. Phys. Lett. 267 (1997) 215–220.
[64] V.A. Neacşu, C. Maxim, A.M. Mădălan, M. Hillebrand, C. González-Arellano, S. Soriano, E. Rentschler, M. Andruh, Polyhedron 150 (2018) 77–82.
[65] M. Jafari, M. Salehi, M. Kubicki, A. Arab, A. Khaleghian, Inorg. Chim. Acta. 462 (2017) 329–335.
[66] S. Chattopadhyay, M.S. Ray, S. Chaudhuri, G. Mukhopadhyay, G. Bocelli, A. Cantoni, A. Ghosh, Inorg. Chim. Acta. 359 (2006) 1367–1375.
[67] B.K. Shaw, M. Das, A. Bhattacharyya, B.N. Ghosh, S. Roy, P. Mandal, K. Rissanen, S. Chattopadhyay, S.K. Saha, RSC Adv. 6 (2016) 22980–22988.
[68] P. Schmid, M. Maier, H. Pfeiffer, A. Belz, L. Henry, A. Friedrich, F. Schönfeld, K. Edkins, U. Schatzschneider, Dalton Trans. 46 (2017) 13386–13396.
[69] S. Bhattacharya, S. Roy, K. Harms, A. Bauzá, A. Frontera, S. Chattopadhyay, Inorg. Chim. Acta. 442 (2016) 16–23.
[70] A. Das, K. Bhattacharya, S. Giri, A. Ghosh, Polyhedron 134 (2017) 295–301.
[71] K. Ghosh, K. Harms, S. Chattopadhyay, Polyhedron 123 (2017) 162–175.
[72] A. Bhattacharyya, K. Harms, S. Chattopadhyay, Inorg. Chem. Commun. 48 (2014) 12–17.
[73] M. Das, S. Chattopadhyay, Polyhedron 50 (2013) 443–451.
[74] K. Ghosh, A. Banerjee, S. Roy, A. Bauzá, A. Frontera, S. Chattopadhyay, Polyhedron 112 (2016) 86–95.
[75] A. Saha, P. Majumdar, S. Goswami, J. Chem. Soc. Dalton Trans. (2000) 1703–1708.
[76] R. Vafazadeh, M. Kashfi, Bull. Korean Chem. Soc. 28 (2007) 1227–1230.
[77] S. Thakurta, R.J. Butcher, G. Pilet, S. Mitra, J. Mol. Struct. 929 (2009) 112–119.
[78] A. Panja, Polyhedron 80 (2014) 81–89.
[79] A. Panja, N.C. Janaa, P. Brandão, New J. Chem. 41 (2017) 9784–9795.
[80] R. Sanyal, X. Zhang, P. Chakraborty, S. Giri, S.K. Chattopadhyay, C. Zhao, D. Das, RSC Adv. 40 (2016) 7388–7398.
[81] S. Albedyhl, M.T. Averbuch-Pouchot, C. Belle, B. Krebs, J.L. Pierre, E. Saint-Aman, S. Torelli, Eur. J. Inorg. Chem. (2001) 1457–1464.
[82] J. Adhikary, I. Majumdar, P. Kundu, H. Kornweitz, H. Kara, D. Das, ChemistrySelect 3 (2018) 1445–1454.
[83] M.E. Alberto, G. Pinto, N. Russo, M. Toscano, Chem. Eur J. 21 (2015) 3736–3745.
[84] V. Katta, S.K. Chowdhury, B.T. Chait, J. Am. Chem. Soc. 112 (1990) 5348–5349.
[85] P. Kebarle, J. Mass Spectrom. 35 (2000) 804–817.
[86] R. Beavis, J. Lindner, J. Grotemeyer, I.M. Atkinson, F.R. Keene, A.E.W. Knight, J. Am. Chem. Soc. 110 (1988) 7535–7536.